npj | materials degradation

Article

Published in partnership with CSCP and USTB

https://doi.org/10.1038/s41529-024-00469-3

Dense Al_2O_3 sealing inhibited high hydrostatic pressure corrosion of Cr/GLC coating

Shuyu Li[1,2], Hao Li[1], Yan Zhang[1], Wei Yang[1], Peng Guo[1] ✉, Xiaowei Li[1,3], Kazuhito Nishimura[1], Peiling Ke[1,2] & Aiying Wang[1,2] ✉

The corrosion failure of amorphous carbon (a-C) coatings is commonly ascribed to the existence of growth microdefects, which serve as pathways for corrosive fluids to permeate the substrate. Atomic layer deposition (ALD) is renowned for its ability to augment the corrosion resistance of metallic materials. Graphite-like carbon (GLC) is one of the amorphous carbon materials dominated by hybridized sp^2-C bonds. In this study, an ALD-deposited Al_2O_3 layer is specially introduced on the Cr/GLC multilayer coating to solve the aforementioned corrosion risk of a-C by taking the sealing conception for defects. Compared to the as-deposited Cr/GLC coating, the coating encapsulated with Al_2O_3 layer depicts the reduction of corrosion current density over two orders of magnitude under a wide pressure range of 0.1 ~ 15 MPa. Particularly, the presence of released Cr^{n+} and Fe^{n+} in the corrosion solution is significantly diminished, accompanying with a small quantity of Al^{n+} generated in sealed coating during corrosion. Microstructural analysis and electrochemical results identified that both the dense Al_2O_3 layer offered strong safeguard for Cr elements released from multilayers, whilst amorphous carbon network inhibited the likelihood chloride penetration induced by partially infiltrated Al_2O_3, which made the synergistic contributions to the enhancement of corrosion resistance for Cr/GLC coating for deep-sea applications.

Marine engineering equipment plays a fundamental role in driving the progress of the maritime economy, where the innovation in state-of-the-art marine relevant machinery and sophisticated vessels has become a focal point for achieving breakthroughs in marine development[1,2]. In general, these cutting-edge systems face a myriad of challenges, including corrosion, tribocorrosion, erosion, biofouling, and the interconnected impact of these factors[3,4]. Particularly, many moving components used for marine engineering not only endure a harsh corrosive environment, but also confront demanding conditions like highly hydrostatic pressure and strongly chloride corrosion during operations, rendering the materials vulnerable to be degraded and dangerous disaster[5–8]. These challenges are particularly decisive for the friction components, such as the ship propeller bearings, submarine buoyancy adjustment part, underwater robot joints, seawater hydraulic system piston pumps, deep-sea drilling lifting and sinking compensation devices. The degradation of corrosion resistance could be clearly evidenced for conventional metallic materials and polymer-based organic coatings under deep-sea environments[9,10]. Consequently, an urgent demand arises for the development of a genre of highly corrosion-resistant coatings combined with other remarkably mechanical and tribological properties.

Amorphous carbon coating (a-C) is a well-known form of amorphous thin film composed of hybridized sp^2 carbon bonds and sp^3 bonds[11]. The graphite-like carbon (GLC) coating is a type of a-C material, especially characterized by a higher content of sp^2 carbon bonds. Thanks to the exceptional attributes of high hardness, superior lubrication and exemplary resistance to corrosion, a-C coatings enable them immense applications in aerospace, automotive, and marine related equipment. More specifically, they are envisioned to serve as an exquisite protective shielding for the vital moving components of offshore equipment[12–16]. However, noted that even these a-C coatings possess outstanding chemical stability in seawater, it is imperative to acknowledge the existence of inherent growth imperfections within the structural network. As an evident observation, such blemishes directly compromise the corrosion resistance and protective performance of a-C films[17]. Conventional methods, notably physical vapor deposition (PVD), employed in the fabrication of a-C coatings often yield the

[1]Key Laboratory of Advanced Marine Materials, Ningbo Institute of Materials Technology and Engineering, Chinese Academy of Sciences, Ningbo 315201, PR China. [2]Center of Materials Science and Optoelectronics Engineering, University of Chinese Academy of Sciences, Beijing 100049, PR China. [3]School of Materials Science and Physics, China University of Mining and Technology, Xuzhou 221116, PR China. ✉e-mail: guopeng@nimte.ac.cn; aywang@nimte.ac.cn

manifestation of growth defects during the deposition process, in which the discernible defects mainly are dominated by nodular defects, pinholes, and even porous penetrations[18]. Once the a-C coatings are exposed to the corrosive media, such defects can easily facilitate the penetration of corrosive electrolytes to substrate, thereby instigating anodic reactions at relevantly vulnerable sites and leading to seriously localized corrosion[19,20]. As a result, it becomes a strong driving force to develop a coating system that exhibits minimal imperfections while upholding superior resistance against corrosion and lubrication.

In order to overcome the aforementioned bottlenecks, various strategies have been attempted to enhance the densification of coatings[20–24]. By introducing the multilayer structure, Li et al. successfully fabricated the Cr/GLC coatings by a hybrid magnetron sputtering technique, where the corrosion resistance of GLC was significantly enhanced due to the suppressed penetration defects at 0.1 MPa, without simultaneous deterioration of other mechanical and tribological properties[22,25]. Nevertheless, different with the atmospheric condition, the protective degradation of coating was subsequently observed under high hydrostatic pressure of 30 MPa because of the defects propagation from the substrate[17]. To evidence this conclusion, the extra-cleaning intervention was further operated to reduce the nodular defects during the deposition of Cr/GLC coatings. The results demonstrated that comparing with pristine Cr/GLC coating, the cleaned coating reduced the corrosion current density about 50 times after immersion into 3.5 wt.% NaCl solution for 300 h with a simulated high hydrostatic pressure (31 MPa)[20]. Very recently, taking the contribution from high power impulse magnetron sputtering (HiPIMS) with high ionization and large incident energy, the densely GLC coating combined with Cr interlayers was achieved. Comparing to Cr/GLC coating deposited by traditional DC magnetron sputtering, HiPIMS-deposited Cr/GLC coatings clearly enhanced the corrosion resistance under a simulated dee-sea environments[24].

Considering the life-time required for offshore equipment in marine, densification of a-C coating is still necessary to prolong the protective performance with inhibition of corrosive penetrating to substrate. Fortunately, atomic layer deposition (ALD) has been an alternatively growing fascination in the context of sealing defects directly[23,26,27]. This technique enables the deposition of a protective oxide film at the atomic-scale, ensuring exceptional uniformity and impeccable densification[28,29]. For instance, Leppäniemi et al. reported the power of ALD layer to modify CrN coatings, in which a remarkable reduction in corrosion current density was indicated. Interestingly, even after the removal of the top ALD layer, the corrosion current density of CrN was remained about 50% lower than that of unsealed CrN, identifying how certain defects in PVD coatings were distinctly sealed by further applied ALD process[26]. This observation acted as undeniable contribution from ALD method in sealing defects of various pinhole or nodular sizes on the surface of coatings.

Taking the conception of sealing advantages, in this study, we fabricated the Cr/GLC multilayered coatings by a hybrid direct current magnetron sputtering deposition system, and introduced an extra Al_2O_3 top-layer over the coating surface by ALD technique. The comprehensive examinations were conducted to identify the evolution of interfacial structure between Al_2O_3 layer and Cr/GLC coatings. The corrosion resistance and electrochemical behavior before and after sealing were comparatively investigated in a high hydrostatic pressure with chloride solutions to emulate the deep-sea marine environment. The scanning vibrating electrode technique (SVET) was particularly employed to address the localized corrosion state occurred at the coated surface for the understanding on the failure mechanism of combined coatings with controlled encapsulating. The Cr/GLC coatings without and with Al_2O_3 sealing were designated as S1 and S2 in the following sections, respectively.

Results and discussion

Microstructural evolution

In order to investigate the changes of chemical structure, the Cr/GLC coating with and without Al_2O_3 sealing was characterized through X-ray photoelectron spectroscopy (XPS) for comparison. Figure 1a shows the XPS spectra of S1 and S2, respectively. Both S1 and S2 samples exhibited C 1s, O

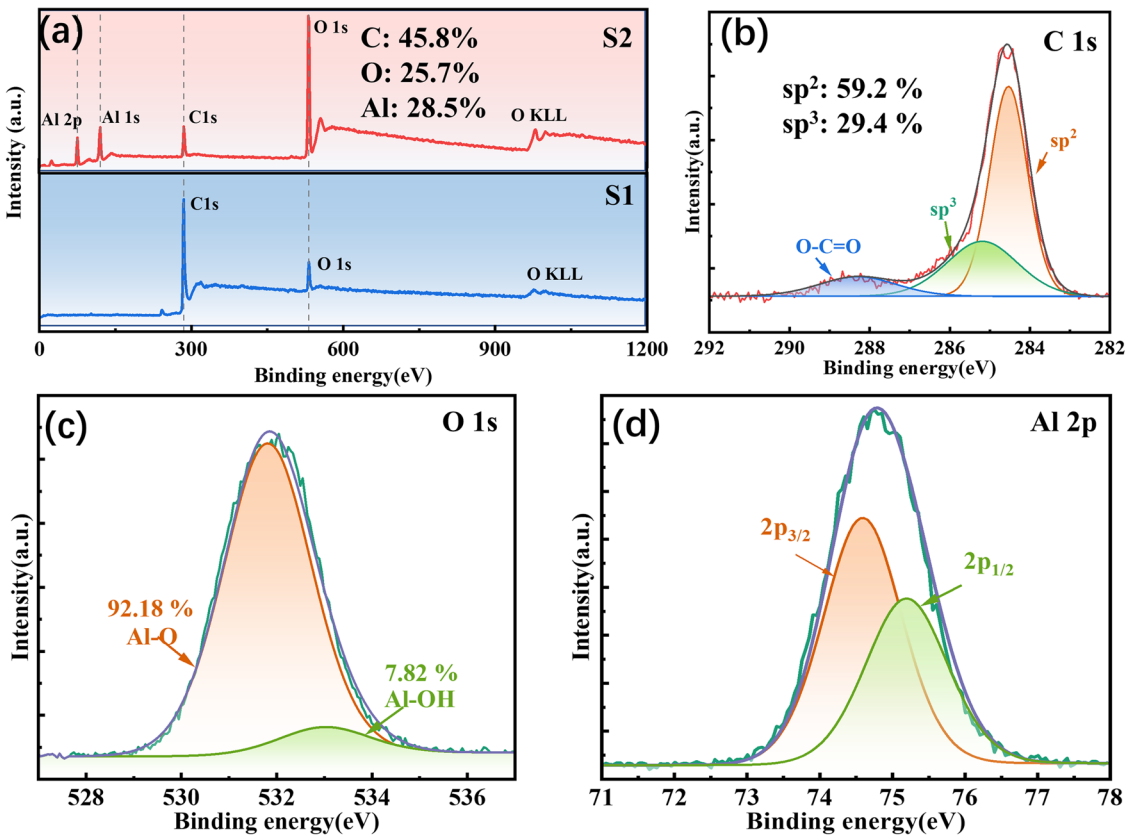

Fig. 1 | The XPS spectra of S1 and S2 with and without Al_2O_3 sealing. a The full spectra, **b** C 1 s, **c** O 1 s, and **d** Al 2p spectra of S2 and corresponding deconvoluted results.

1s, and O KLL peaks in the respective spectra correspondingly. Noted that, however, the spectrum of the S2 coating revealed the presence of Al 1s and 2p peaks, accompanying with a significantly increment in the intensity of O 1s peak. This observation strongly suggested that the deposition of Al_2O_3 layer was successfully achieved on the surface of Cr/GLC multilayer coating. As evidenced in Fig. 1b–d, all the C 1s, O 1s, and Al 2p spectra obtained from S2 were primarily originated from the topmost layer combined with Cr/GLC coating. The XPS calibration using the binding energy of C1s (284.8 eV). The C 1s The C 1s spectrum was further deconvoluted into three distinct components: a sp^3 C-C bond at 285.2 ± 0.2 eV, a sp^2 C = C bond at 284.4 ± 0.2 eV, and an O-C = O bond assigned to 288.2 ± 0.2 eV[17]. Therefore, the percentages of sp^2, sp^3, and O-C = O bonds were determined to be 59.19%, 29.44%, and 11.37%, respectively. Likewise, the O 1 s spectrum underwent deconvolution with two different peaks: Al-O at 531.8 ± 0.2 eV and Al-OH at 533.4 ± 0.2 eV. During the reaction between trimethylaluminum (TMA) and water (H_2O), the methyl groups ($-CH_3$) were replaced by hydroxyl groups (-OH), leading to the formation of Al-OH bonds with CH_4. Nevertheless, due to incomplete reaction of TMA, some of Al-OH bonds were trapped within the Al_2O_3 structure[30]. The contents of Al-O and Al-OH bonds were 92.18% and 7.82%, respectively. The dominant peak displayed in the Al 2p spectrum at approximately 74.8 ± 0.2 eV could be further resolved into Al $2p_{3/2}$ at 74.5 ± 0.2 eV and Al $2p_{1/2}$ at 75.2 ± 0.2 eV. These values also proposed the presence of O-Al-O bonds. Based on the above analysis, it could be reasonable said that both O and Al species emerged on the surface of the Cr/GLC coating, predominantly in the form of Al_2O_3 phases, corresponding to the successful encapsulating of Al_2O_3 for Cr/GLC coating[31].

Surface and cross-sectional morphologies

Figure 2 shows the representative transmission electron microscopy (TEM) and elemental mapping of the Cr/GLC coating with Al_2O_3 sealing layer. The selection image was specifically focused on the defect location for evaluating the encapsulated influence of Al_2O_3. Figure 2a depicts the presence of penetration defects inclined towards the edge of the coating, in which dark gray and light gray shades illustrated the Al_2O_3 layer and GLC, respectively. Clearly, the Al_2O_3 layer exhibited the exceptional uniformity with a thickness of approximately 45 nm. In addition, noted that the Al_2O_3 layer represented the typical amorphous characteristics of short-range order and long-range disorder, which was also evidenced by the diffused halo diffraction rings. Moreover, this feature could be identified from the fast Fourier Transform (FFT) analysis of the TEM images in Fig. 2a. The selected area electron diffraction (SAED) results of the Al_2O_3 layer revealed the typical amorphous structures for the outmost encapsulation. The Cr/GLC coating demonstrated a clear laminar structure with a well-established Cr/C interface (Fig. 2b). According to the localized magnification of interfaces between Al_2O_3 and GLC layers, the distribution of Cr and O elements were bonded coherently, owing to the formation of chromium oxide through their interactions amidst ambient air. Meanwhile, both O and Al elements were detected above the GLC layer, extending into the next Cr layer. This phenomenon strongly suggested that the Al_2O_3 not only was densely deposited the surface of the Cr/GLC coating but also infiltrated the defects with an outstandingly penetrative effect without expectation.

Figure 3 illustrates the plan view morphology and three-dimensional morphology image by atomic force microscopy (AFM) measurement for S1 and S2 samples. All the coatings illustrated a continuous, uniform and smooth surface morphology regardless of Al_2O_3 encapsulating, despite the cauliflower shaped protrusions were visible from the coating surfaces. Due to the continued growth of amorphous carbon along the transition layer or substrate surface structure. For S1 and S2 samples, the R_q value of coating was slighted reduced from 13.3 nm to 12.3 nm before and after Al_2O_3 sealing process. The reason could be arisen from the densely amorphous overcoated Al_2O_3 facilitated by ALD technique. Since atomic layer deposition (ALD) technology is a conformal process to produce the continuously dense Al_2O_3 layer[32], it can be suspected that introducing the Al_2O_3 sealing layer enables the defect encapsulating for the pristine Cr/GLC coating, consequently benefiting the smoothness increment in coating. However, the 45 nm-thickness Al_2O_3 layer was too thin to conquer the cluster-shape surface of Cr/GLC coating, as identified by the slight decrease of R_q only around 1 nm.

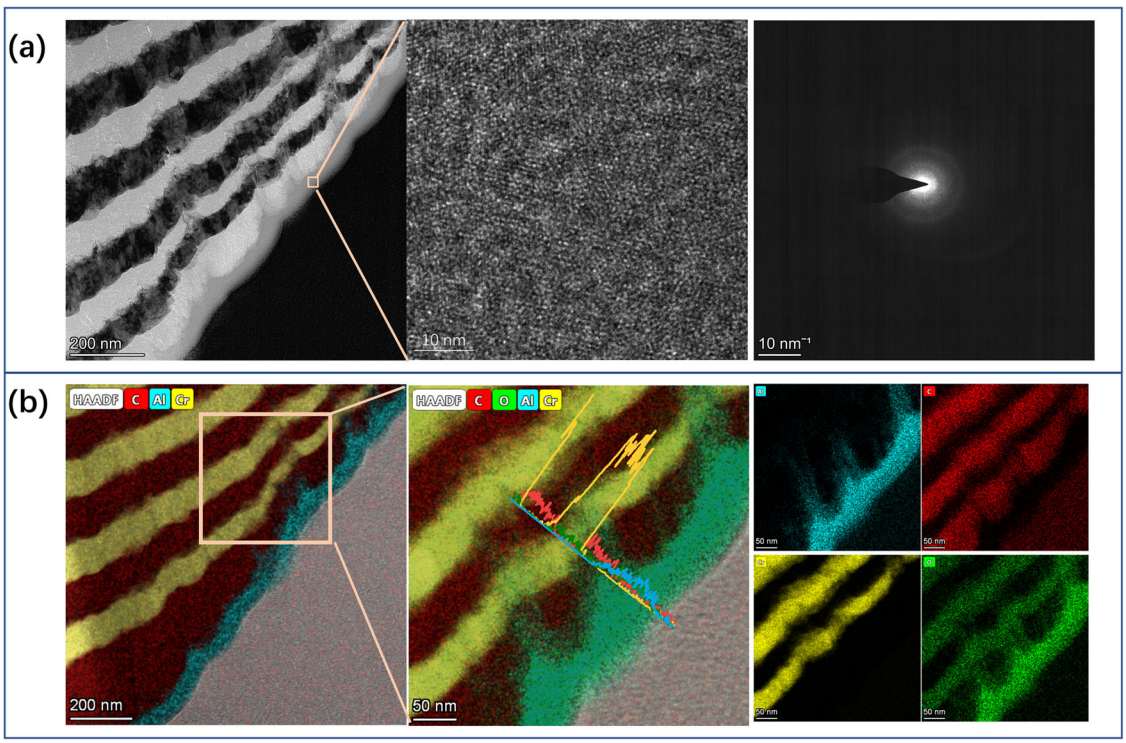

Fig. 2 | The TEM and elemental mapping morphology of S2. a Cross-sectional image of HRTEM with FFT analysis and selected area electron diffraction (SAED), and **b** Elemental mapping of S2.

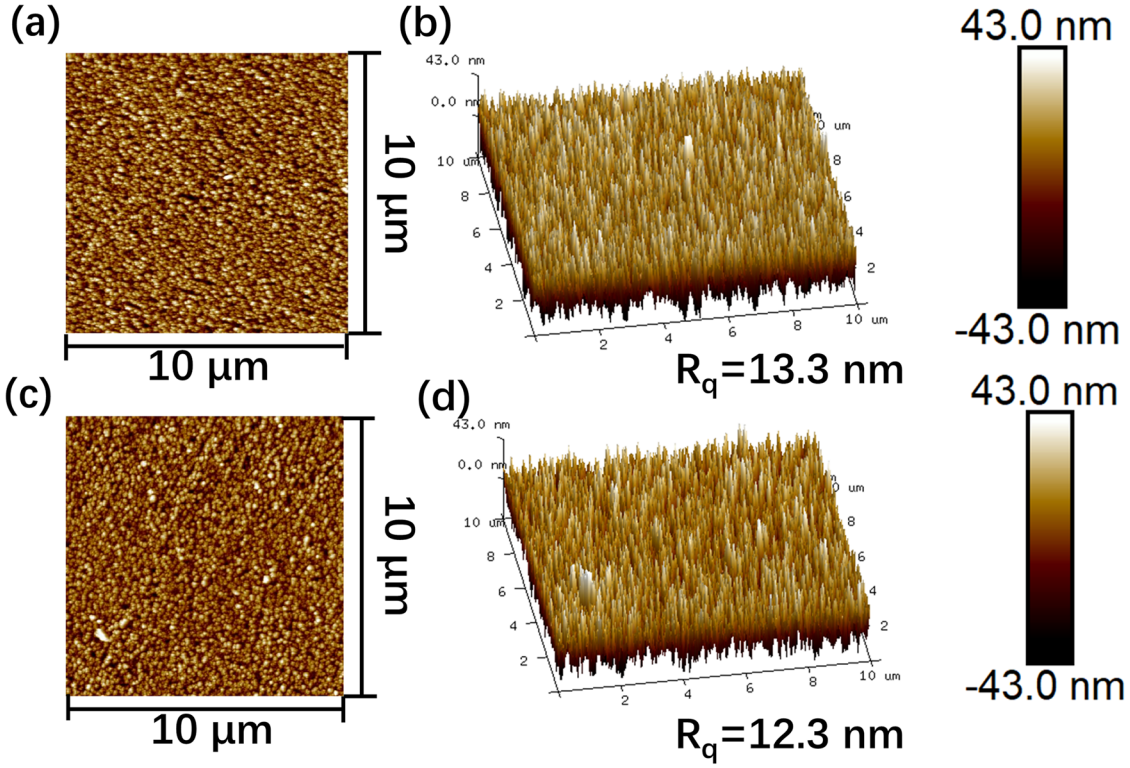

Fig. 3 | The AFM images and surface roughness of Cr/GLC coating. a The two-dimensional surface morphology of S1, **b** The two-dimensional surface morphology of S2, **c** The three-dimensional topographic AFM images and the corresponding R_q roughness values of S1, and **d** The three-dimensional topographic AFM images and the corresponding R_q roughness values of S2.

EIS analysis

To address the effect of Al_2O_3 sealing on the corrosion resistance of the Cr/GLC coating, EIS analysis was performed specially in a 3.5 wt. % NaCl solution under pressures of 0.1 MPa and 15 MPa. Figure 4a, b show the Nyquist plots and Bode plots, respectively, along with the respective fitted curves. All Nyquist plots exhibited a striking capacitance loop alongside a linear segment spanning the entire frequency spectrum, suggesting a defensive capacity against hydrostatic corrosion. From the enlarged image, the arc radius of the capacitances for both S1 and S2 decreased at pressure of 15 MPa than those at 0.1 MPa. However, comparing to S1 sample without sealing, the S2 sample still maintained a larger capacitance arc radius, indicating the outstanding corrosion resistance even under high hydrostatic pressure. Generally, the EIS displayed a substantial phase angle (φ), indicative of the material's strong capacitance characteristic, particularly in the intermediate frequency phase angle[33]. For the S1 sample lacking Al_2O_3 sealing, at 0.1 MPa, the φ value approached approximately 80° within the mid-frequency region, denoting commendable corrosion resistance. Nevertheless, when subjected to a higher hydrostatic pressure of 15 MPa, a noticeable overall downward shift in φ occurred due to the facile permeation of corrosive fluid through surface defects, thereby deteriorating the protective capability of the coating. In contrast, following the Al_2O_3 sealing of the Cr/GLC surface, the φ value maintained near 90° across the frequency range in 0.01 ~ 10,000 Hz at 0.1 MPa, revealing the outstanding corrosion stability. Increasing the hydrostatic pressure to 15 MPa caused a distinct decline in the φ value at 2 Hz for S2, probably due to the corrosive fluctuations from the encapsulated Al_2O_3 layer. The hydrostatic pressure contributed to the deterioration of the Al_2O_3 layer by augmenting the activity of adsorbed Cl^- ions on the sample surface, thus facilitating the dissolution of Al_2O_3. As the hydrostatic pressure ascended from 0.1 MPa to 15 MPa, the impedance values of S1 and S2 decreased from 1.79×10^6 Ω·cm^2 and 3.89×10^8 Ω·cm^2 to 6.79×10^5 Ω·cm^2 and 6.86×10^7 Ω·cm^2, respectively. Moreover, it was worth mentioning that the impedance values of S2 under different hydrostatic pressures were larger than those of S1, indicating that the hermeticity of ALD-deposited Al_2O_3 film greatly improved the corrosion resistance of the Cr/GLC coating at pressure of 0.1 ~ 15 MPa.

The EIS fitting data for S1 and S2 were fitted using the equivalent circuit, as shown in the inset of Fig. 4a. In this circuit, R_s symbolized the electrolyte resistance, R_{ct} represented the charge transfer resistance, and CPE_{dll} was assigned to the double-layer capacitance. Additionally, R_{po} and CPE_c denoted the pore resistance and capacitance of the coating, respectively. To account for the "scattering effect" in the coating system, a constant phase element (*CPE*) was employed instead of a pure capacitance[17]. The values of the electric double layer capacitance, CPE_{dll}, were calculated by Brug's formula[34]. The values of the CPE_c were calculated based on the work from Hsu's and Mansfeld's studies[35]. Table 1 presented the fitting parameters obtained from the EIS analysis. CPE_c, which stands for capacitance of the coating, was widely recognized in relation to the porosity of the coating. Referring to the empirical equations[20], a higher magnitude of CPE_c signified a rapid corrosion process during immersion, which could be intricately linked to the chemical composition and microstructure of the multilayer coating system. Following the 15 MPa immersion, the CPE_c of the S1 experienced an elevation from 7.88×10^{-6} F·cm^{-2} to 1.08×10^{-6} F·cm^{-2}. On the other hand, the CPE_c of S2 increased from 3.89×10^{-8} F·cm^{-2} to 1.69×10^{-7} F·cm^{-2}. Since the CPE_c in this context was largely influenced by the exposed area of the active region and the porosity of the coating, the findings revealed that the Al_2O_3 sealing effectively mitigated defects in the coating, thus diminishing the potential for interface corrosion between the Cr layer and the GLC layer[24]. Taking into consideration the evolution of CPE_{dll}, Table 1 elucidated the corrosive reaction observed between the substrate and coating. Compared to S1, S2 manifested a smaller value of CPE_{dll} under the influence of high hydrostatic pressure amounting to 15 MPa, implying a comparatively feeble corrosion reaction transpiring at the interface[17].

At a hydrostatic pressure of 15 MPa, the value of R_{po} for S1 was surprisingly low, approximately five orders of magnitude smaller than that at 0.1 MPa. This observation proposed the existence of defects in the Cr/GLC

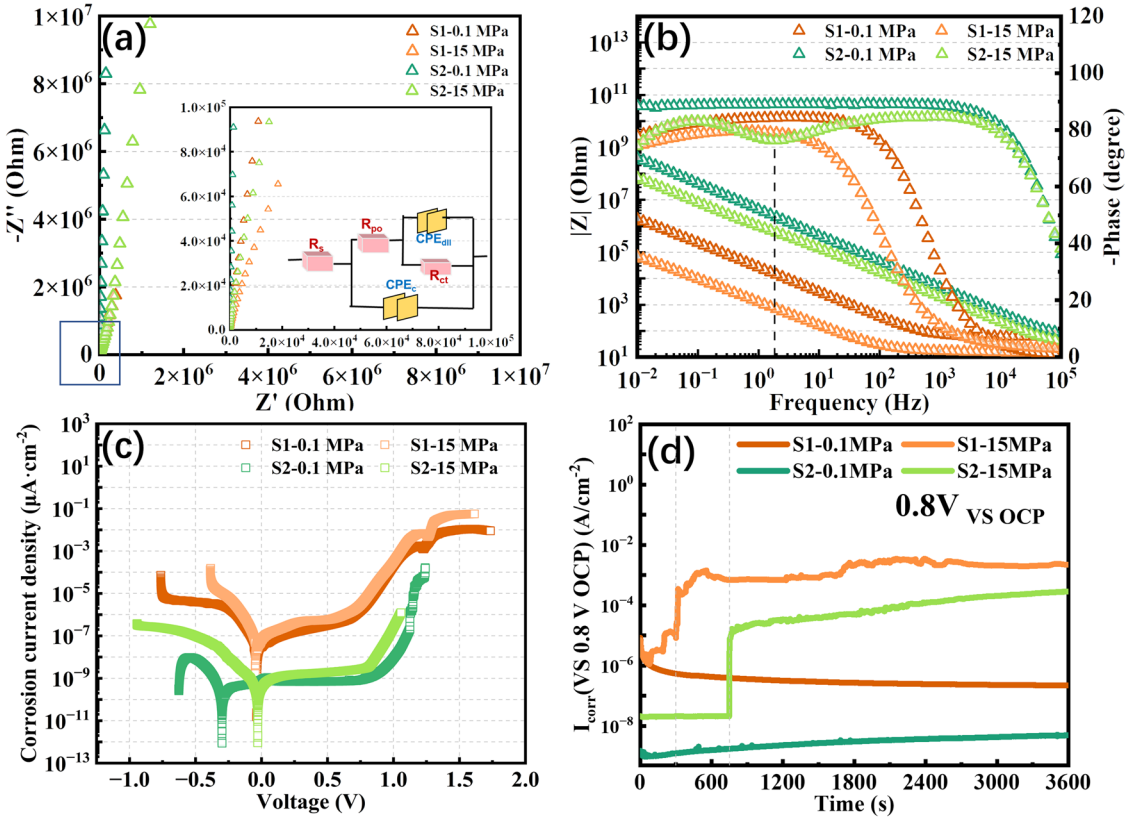

Fig. 4 | The corrosion test of S1 and S2. a Nyquist plots, **b** Bode plots, **c** potentiodynamic polarization, and **d** potentiostatic polarization.

coatings, which could yield the penetration of corrosive fluids under high hydrostatic pressures. Conversely, the Cr/GLC coating sealed with Al_2O_3 layer displayed virtually no reduction in R_{po} under 15 MPa. In general, it was empirically known that R_{ct} was signified the rate of charge transfer at the interface between substrate and electrolyte solution, the higher values of R_{ct} indicated a slower corrosion reaction within the system. In comparison to S1, the value of R_{ct} for S2 was three orders of magnitude larger under different hydrostatic pressures, reflective of the excellent ability to impede the flow of corrosive fluids. According to these aforementioned variations in the fitting results, S2 sample possessed an extremely high level of compactness and performed the exemplary resistance against chloride corrosion for deep-sea application due to the encapsulated Al_2O_3 layer. Meanwhile, Dense Al_2O_3 mitigated the potential for interface corrosion between the Cr layer and the GLC layer by minimizing the infiltration of corrosive fluids.

Table 1 | The EIS fitting results of Cr/GLC without and with 45 nm Al_2O_3

Coatings Hydrostatic pressure	As-deposited 0.1 MPa	As-deposited 15 MPa	Al_2O_3-45 nm 0.1 MPa	Al_2O_3-45 nm 15 MPa
R_s (Ω·cm^2)	58.43	13.75	64.76	28.79
CPE_c (F·cm^{-2})	7.88×10^{-6}	1.08×10^{-4}	3.89×10^{-8}	1.69×10^{-7}
R_{po} (Ω·cm^2)	150.800	4.328	5.71×10^{6}	1.40×10^{6}
CPE_{dll} (F·cm^{-2})	1.68×10^{-9}	5.66×10^{-5}	1.24×10^{-11}	2.36×10^{-8}
R_{ct} (Ω·cm^2)	3.68×10^{7}	6.20×10^{5}	7.06×10^{10}	3.87×10^{8}
I_{corr} (10^{-7} A·cm^{-2})	7.38	9.25	0.0075	0.0139
Polarization Resistance (10^6 Ω·cm^2)	0.988	0.571	767	120
Pitting potential (V)	-	-	1.0	0.90

Polarization tests

Figure 4c shows the potentiodynamic polarization curves for samples S1 and S2, under hydrostatic pressures of 0.1 MPa and 15 MPa, respectively. The relevant fitting outcomes are also presented in Table 1. For comparison, it was evident that at 0.1 MPa, the i_{corr} values for S1 was stabilized at 7.38×10^{-7} A·cm^{-2}, whereas that of S2 stabilized at a significantly lower value of 7.5×10^{-10} A·cm^{-2}, approximately three orders of magnitude below that of S1. In this aspect, it could be said that the capability of corrosion resistance in S2 sample was much stronger than that in S1 case. Nevertheless, with increment of the hydrostatic pressure to 15 MPa, the corresponding i_{corr} values for both S1 and S2 increased to 9.25×10^{-7} A·cm^{-2} and 1.39×10^{-9} A·cm^{-2}, respectively, indicating a slight decline in the corrosion resistance of both samples.

Furthermore, the corrosion potential (E_{corr}) for sample S2 at 0.1 MPa was determined to be −0.304 V, which displayed a cathodic shift when compared to sample S1 at both 0.1 MPa and 15 MPa. The reason behind of this phenomenon could be attributed to the obstructive benefits of S2 on the diffusion of chloride, water and dissolved oxygen, resulting in reduced cathodic current and a shift towards the cathodic region of the E_{corr} at 0.1 MPa[36]. Such observation further confirmed that the S2 specimen possessed the lower defect density and superior capability in impeding the permeation of water and dissolved oxygen. Noted that, however, under the hydrostatic pressure of 15 MPa, the E_{corr} of S2 experienced an anodic shift in contrast to that at 0.1 MPa, primarily because of the accelerated penetration of dissolved oxygen and water combined with chloride ions[17]. Additionally, the corrosion current densities of cathodic domain for both S1 and S2 at 0.1 MPa were inferior to those observed at 15 MPa, which agreed well with the aforementioned analysis. Notably, in the cathodic region, the discussion was mainly revolved around the reduction of dissolved oxygen and water in

neutral solutions, rather than chloride ions, as they were the principal factors driving cathodic corrosion[36].

In the anodic region, the corrosion current density (i_{corr}) of sample S1 exhibited a slight incline, lacking of any obvious indications of pitting corrosion, epitomizing the typical behavior observed in the anodic region of GLC coatings. Prior to reaching a voltage of 1.1 V at both 0.1 MPa and 15 MPa, there was negligible disparity in the i_{corr} values of S1. Beyond of 1.1 V, however, the i_{corr} considerably escalated at 15 MPa, indicating the accelerated vulnerability of the Cr/GLC coating to failure under high hydrostatic pressure. This vulnerability had already been substantiated in our prior research[17,24]. In contrast, for sample S2 possessed an Al_2O_3 seal, a corrosion behavior resembling pitting was observed on account of the Al_2O_3 surface in the anodic region. In particular, a gradual corrosion that extended from the corrosion potential (E_{corr}) to the pitting potential (E_{pit}) was distinctly illustrated in anodic region. Generally, E_{pit} refers to the potential at which there is a pronounced surge in anodic current, implying the commencement of stable pit growth. Nevertheless, in the case of S2, the curve displayed a gentler inflection at 0.1 MPa after 0.9 V. The reason might be ascribed to the predominant role played by inert carbon matrix in this corrosion process[20]. At 15 MPa, the pitting corrosion of S2 became more prominent due to the stimulated activity of corrosive Cl^- ions under high hydrostatic pressure, which intensified the attack on Al_2O_3[37]. The corrosion processes could be understood according to the following chemical reaction equations:

$$Al_2O_3 + 3H_2O \rightarrow 2Al(OH)_3 \quad (1)$$

$$Al(OH)_3 + Cl^- \rightarrow Al(OH)_2Cl + OH^- \quad (2)$$

$$Al(OH)_2Cl + OH^- + Cl^- \rightarrow Al(OH)Cl_2 + 2OH^- \quad (3)$$

$$Al(OH)Cl_2 + 2OH^- + Cl^- \rightarrow AlCl_3 + 3OH^- \quad (4)$$

To investigate the corrosion mechanism of the Cr/GLC coating caused by Al_2O_3 sealing, potentiostatic polarization was further employed, providing a more comprehensive representation of the samples' corrosion under identical conditions. Figure 4d depicted the corrosion current densities (I_{corr}, 0.8 V $_{VS\ Ag/AgCl}$) of various samples. At pressure of 0.1 MPa, both S1 and S2 exhibited smooth curves, suggesting their good stability. For the clear observation, the enlarged image for the first 50 s during test was inserted in Fig. 4d as well. However, the I_{corr} of S2 was nearly three orders of magnitude lower than that of S1, confirming not only the excellent barrier properties of densely amorphous Al_2O_3 but also its significant passivation effect. With increase of hydrostatic pressure to 15 MPa, the I_{corr} of S1 demonstrated the fluctuations at 100 s, followed by a stepwise increase and an instantaneous surge to nearly 10^{-3} A/cm^{-2} at 300 s. This phenomenon indicated the deterioration of the coating and the consequential corrosion from substrate. Interestingly, such behavior was absent in the S2 sample, where the I_{corr} exhibited a gradual and consistent rise over 850 s, implying the absence of severe substrate corrosion.

Surface morphology and solution ions content after polarization

Figure 5 shows the surface morphologies of S1 and S2 following potentiostatic polarization, as observed through scanning electron microscopy (SEM) and optical microscope (OM) measurement. It was evident that S2 possessed an immaculate surface even after undergoing corrosion at a high voltage of 0.8 V. Conversely, S1 illustrated the surface with noticeable corrosion pits, in which the center of these pits appeared as hollow and the surrounding coating displayed the clear downward collapse. The formation of such corrosion pits could be originated from the initial expansion of substrate corrosion caused by a minute defect, resulting in the loss of interfacial adhesion between the coating and the substrate. Notably, the interior of these corrosion pits exceeded the dimensions captured by SEM. Moreover, Table 2 demonstrates the ion concentrations released in the

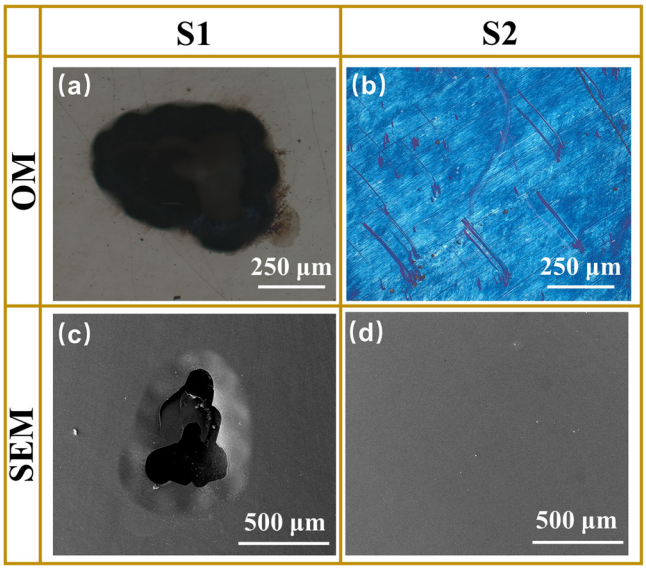

Fig. 5 | SEM and OM surface morphologies of the S1 and S2 after the potentiostatic polarization. a OM of S1, **b** OM of S2, **c** SEM of S1, **d** SEM of S2.

Table 2 | Ion concentration in solution after polarization (0.8 V) of S1 and S2

Sample	Fe^{n+}(mg/L)	Cr^{n+}(mg/L)	Al^{n+}(mg/L)
S1 (as-deposited)	0.4997	0.1324	0
S2 (with Al_2O_3 sealing)	0.0022	0.001	0.0226

solution following 0.8 V corrosion at 0.1 MPa after sealing the defects with Al_2O_3. The released ion content in the solution was collected and analyzed by ICP-OES technique. A significant two-order reduction in Fe^{n+} and Cr^{n+} ions was achieved within the solution for S2 than those for S1. This served as evidence that the Al_2O_3 sealing could significantly prevent the penetration of corrosive Cl^- into the substrate, but also strongly inhibited the corrosion of the Cr within the multilayer. Consequently, the liquid after potentiostatic polarization presented a higher concentration of Al^{n+} ions compared to Fe^{n+} and Cr^{n+} ions due to the dissolution of Al_2O_3.

XPS after polarization

Based on the results obtained from the above experiments, the surface structure of the coating after corrosion was analyzed and summarized using XPS technology. Figure 6 shows the Al 2p and O 1s spectra after potentiostatic polarization corrosion. The shape of peaks for both spectra was the same as that in Fig. 1. The fitting results of Al 2p peak in Fig. 6a show that there was no significant change in the curve before and after corrosion. This indicated that there were still O-Al-O bonds on the surface of the coating, meaning that there was still Al_2O_3 protection on the surface. The fitting results of O 1s peak in Fig. 6b. The main peak of the O 1s spectrum remained at 531.8 eV, with no significant shift. A small peak at 533 ± 0.2 eV was fitted, and research had shown that this peak was mainly Al-OH. Before immersion, the fitted content of Al-OH was approximately 7.82%, mainly generated during the ALD reaction. After immersion, the fitted content of Al-OH increased to 21.16%. This result indicated that due to immersion in 3.5 wt.% NaCl, Al_2O_3 had undergone slight changes, generating more Al-OH. The specific reaction process is shown in Eq. (1–4). This also confirmed the cause of the change in polarization curve.

Local electrochemical analysis

It is empirically known that the samples immersed in an electrolyte solution generate an ionic current as a result of the existence of a cathode and anode

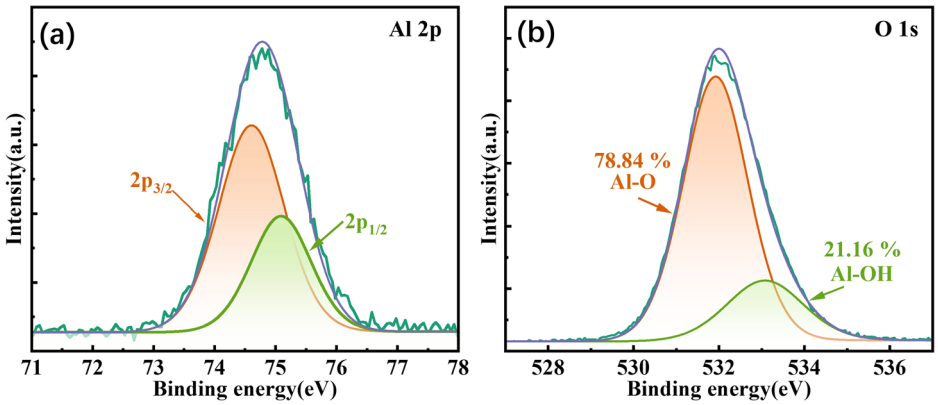

Fig. 6 | The XPS spectra of S2 with Al_2O_3 sealing after potentiostatic polarization. a Al 2p, and **b** O 1s spectra and corresponding deconvoluted results.

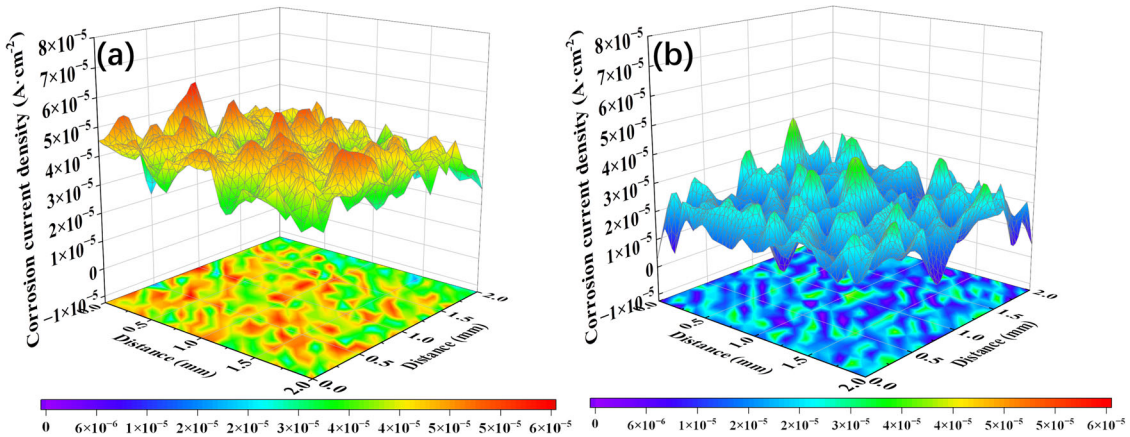

Fig. 7 | The local corrosion current density of coatings. a SVET maps of S1, and **b** SVET maps of S2.

on the surface, thus giving rise to a potential gradient. Employing the SVET technique, it is possible to investigate the localized corrosion performance of a material by utilizing a conducting probe to quantify the magnitude of the potential difference within the solution, which thereby can acquire information on the ionic current. Figure 7 shows the SVET mappings of S1 and S2 for comparison. The potential difference obtained through the SVET approach was subsequently converted using Eq. (5) to derive the corrosion current density.

$$\Delta\varphi = -\frac{i}{\sigma} \tag{5}$$

Where, σ (S/m) was the electrical conductivity of the NaCl electrolyte solution (6.5 S/m), Δφ was the potential difference between the surface and the probe, and i was assigned to the relative corrosion current density.

For a certain sample, the corrosion current density could be stemmed from an inherent self-corrosion process, corresponding itself in a comparative manner. According to the SVET observations, both S1 and S2 displayed a consistent undulation, lacking of any discernible imperfections on surface. Furthermore, different with the large diversity of corrosion current density for S1 sample, the diminished variation of corrosion current density distributed in S2 alluded to a minute potential difference between the surface and the probe, suggestive of an improved self-corrosion potential on the sealed surface. These results conveyed that the inclusion of Al_2O_3 significantly reduced the propensity for self-corrosion in the encapsulated Cr/GLC coatings, with sealing accomplished at an exceedingly microscopic scale and obviating visible pinholes.

In brief, the Cr/GLC multilayer coating with Al_2O_3 sealing strategy possessed the exceptional corrosion resistance and effectively mitigated the corrosion of the Cr layer, consequently minimizing the likelihood of interfacial galvanic corrosion. The primary reason behind this phenomenon lied in the seamless integration of densely amorphous Al_2O_3, which impeccably filled the microdefects within the deposited Cr/GLC structure. Moreover, the ALD technique triumphed over the defects influence easily induced by physical vapor deposition. For easier understanding, Fig. 8 shows the schematic diagram elucidating the mechanism by which corrosion was distinctly impeded. Under conditions of elevated hydrostatic pressure to 15 MPa, the presence of ALD-deposited amorphous Al_2O_3 acted as a densely barrier, inhibiting the penetration of corrosive Cl^- ions into the Cr layer within coating structure, thereby guaranteeing the uninterrupted functionality of the Cr layer, without standing the potential dissolution and pitting corrosion of Al_2O_3 even at high hydrostatic pressures. However, the a-C coating presented a splendidly substantial obstruction layer for the substrate, whilst Al_2O_3 strongly mitigated the defects inherent in the amorphous carbon matrix. Simultaneously, the a-C beheld the potential to safeguard the penetrated alumina within the coating. Such synergistic contribution of these two factors favored the unparalleled fortification upon metallic systems by Cr/GLC multilayer coating with encapsulated dense Al_2O_3.

In this study, Al_2O_3 film fabricated using atomic layer deposition (ALD) technique was introduced to rectify the growth imperfections of the Cr/GLC multilayer coating deposited by hybrid DC magnetron sputtering. The results demonstrated that the Al_2O_3 film was not only amorphous and uniform distributed over the coating surface, but also could be flawlessly embedded within the amorphous GLC topmost layer and adjacent crystalline Cr layers. When exposed to a voltage of 0.8 V, the current density of the as-deposited Cr/GLC coating dramatically increased after 300 s, leading to significant corrosion failure. Nevertheless, thanks to the densely

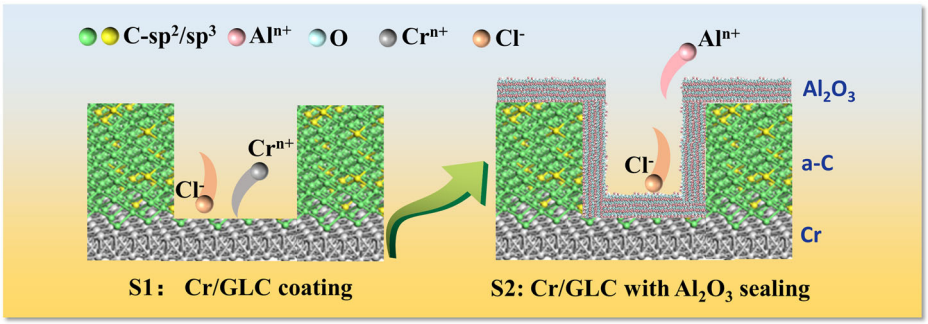

Fig. 8 | Schematic diagram of the corrosion protection mechanism of Cr/GLC coatings without and with Al_2O_3 sealing.

Table 3 | Chemical composition of 17-4 PH stainless steel

Element	C	Mn	Si	Cr	Ni	P	S	Cu	Nb+Ta
Content (wt.%)	≤0.07	≤1.00	≤1.00	15.5~17.5	3.0~5.0	≤0.04	≤0.03	3.0~5.0	0.15~0.45

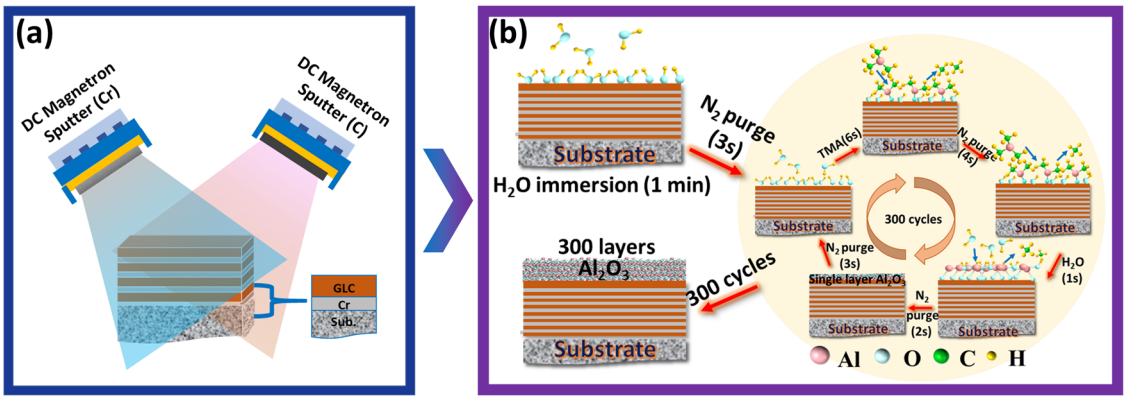

Fig. 9 | The schematic diagram of the deposition processes. a The preparation of Cr/GLC coating by magnetron sputtering, and **b** The process of ALD-Al_2O_3 sealing modification.

incorporation of Al_2O_3 as a diffusion barrier for chloride medium, the Cr/GLC coating encapsulated by amorphous Al_2O_3 remarkably enhanced the corrosion resistance. Correspondingly, a corrosion current density of i_{corr} value at 1.39×10^{-9} A/cm^{-2} was obtained, which was much lower than that of un-sealed coating at 9.25×10^{-7} A/cm^{-2} under the pressure of 15 MPa. The outstanding sealed properties of ALD technique, combined with the inherent passivation capabilities of amorphous alumina, significantly suppressed the likelihood of penetration of corrosive solutions into the coating, thereby augmenting the corrosion resistance of DLC coating in stimulated deep-sea environments. It is worth noting that considering the influence of density and porosity for coatings deposited by traditional PVD techniques, the implementation of ALD sealing emerges as a compelling alternative strategy to modify coating intrinsic defects, potentially yielding the desired outstanding corrosion resistance for advanced carbon coatings without deteriorating the relevant mechanical and tribological performance.

Methods

Coating preparation

The Cr/GLC multilayer coating was initially fabricated on a 17-4 PH stainless steel substrate using a home-made hybrid direct current magnetron sputtering technology. The detailed chemical composition for used 17-4PH substrate was showed in Table 3. The rectangular Cr target (purity of 99.9%) and graphite target (purity of 99.99%) were used as sputtered sources for discharged Cr and C plasma, respectively. The identical dimension of targets was about 380 mm × 100 mm × 7 mm. During deposition, the sputtering current supplied to the Cr target and C target was set at 3.5 A and 3.0 A in DC mode, corresponding to the power of 1700 W and 2000 W, respectively. Argon working gas was introduced to the chamber with a flow rate of 55 sccm. The deposition process for the Cr/GLC coating could be clarified to a stage based on our previous studies[17,22,24,25]. Briefly, the first stage involved depositing Cr and Cr_xN for a duration of 4 min each. The second stage included applying the GLC coating for 22 min, followed by the deposition of the Cr intermediate layer for 4 min. This GLC and Cr layer deposition process was repeated for 7 cycles. Finally, a top layer of thickened GLC was deposited for 50 min to enhance the coating's capacity for bearing friction. Subsequently, the as-deposited Cr/GLC surface was sealed with an Al_2O_3 layer utilizing the ALD technique. Figure 9 illustrates the schematic diagram of the Cr/GLC coating deposition and the relevant ALD process, wherein trimethylaluminum (TMA) and H_2O were utilized as the reaction gases, while N_2 was employed to eliminate impurities and poorly adsorbed substances. Before introducing it into the ALD chamber, the Cr/GLC coating must be immersed in water for 60 s in order to generate surface hydroxyl groups. During the ALD procedure, the chamber's heating rod and the gas pipes' heating tape were individually heated to 250 °C and 60 °C, followed by preheating the chamber and reaction gas for 2 h. Thereafter, the gases were alternately energized and introduced into the chamber in the next sequence: N_2 (3 s), TMA (6 s), N_2 (4 s), H_2O (1 s), and N_2 (2 s), repeating for a total of 300 cycles to achieve a Al_2O_3-sealed coating. For convenience, the

Cr/GLC coatings without and with Al_2O_3 sealing were designated as S1 and S2 in the following sections, respectively.

Structural characterization

The chemical composition of coatings was tested using X-ray photoelectron spectroscopy (XPS, Axis Ultra DLD, Japan) with mono-chromated Al (mono) Kα irradiation at a pass energy of 160 eV. The imaging spatial resolution of XPS was less than 3 μm. Furthermore, the high resolution XPS regions in the Cr/GLC coating with Al_2O_3 sealing were determined from the C 1s, O 1s, and Al 2p XPS spectra using a combination of a Gaussian (30%) and a Lorentzian (70%) function after subtracting Shirley background. The microstructure of the Cr/GLC coating with Al_2O_3 sealing was examined using high-resolution transmission electron microscopy (TEM, Talos F200x, US) operating at a voltage of 200 kV. The samples for TEM were prepared by focused ion beam (FIB, Carl Zeiss, Auriga, Germany). Firstly, the Pt layer was deposited on the surface to protect the coating sample. Secondly, the Ga ion beam was conducted to mill the sample to acquire the standard feature for TEM vision. Atomic force microscopy (AFM, Dimension 3100 V, Vecco, US) in a tapping mode was used characterize the surface topography and roughness of Cr/GLC with and without Al_2O_3 sealing. Particularly, root-mean-square roughness (R_q) of the samples was calculated from 512 × 512 surface height data points obtained from a 10 μm × 10 μm scanning area based on NanoScope Analysis 2.0 software. The surface morphology of the coating after corrosion tests was comprehensively investigated by scanning electron microscopy (SEM, FEI Quanta FEG 250, USA) operating at a voltage of 15 kV with a secondary electron imaging mode. In addition, surface morphology was also observed using the optical microscope for larger identification (OM, Leica, Germany).

Electrochemical and immersion tests

The electrochemical impedance spectrum (EIS), potentiodynamic polarization and potentiostatic polarization were performed for the coating utilizing the Reference 600+ workstation (Gamry, USA) equipped with a three-electrode system. The EIS measurements were conducted within the frequency range of 100 kHz to 0.01 Hz. The amplitude was 10 mV. For the potentiodynamic polarization tests, a sweep rate of 1 $mV{\cdot}s^{-1}$ was employed, applying a potential range from −1.0 V to 1.5 V vs. OCP. During potentiostatic polarization, a constant potential of 0.8 V was maintained for a duration of 1 h. After one hour potentiostatic test, the corrosion solution was subsequently collected and the concentrations of released Fe^{n+}, Cr^{n+}, and Al^{n+} ions were quantified using an inductively coupled plasma emission spectrometer (ICP-OES, Agilent, USA). To investigate the localized corrosion current density surrounding the defect, the scanning vibrating electrode technique (SVET) was especially employed through the introduction of the micro scanning electrochemical workstation (VersaSCAN, AMETEK, USA). In this regard, the test area encompassed dimensions of 2000 μm × 2000 μm, while maintaining a separation distance of 100 μm between the microelectrode probe and the working electrode. The vibration amplitude was set at 30 μm, operating at a frequency of 80 Hz. Furthermore, immersion tests were executed using the autoclave corrosion test system (CORTEST Inc., USA) to explore the electrochemical behavior of the coatings under high hydrostatic pressure with emulated 3.5 wt.% NaCl solution for 5 h.

Data availability

The data are available from the corresponding author on reasonable request.

Received: 15 January 2024; Accepted: 24 April 2024;
Published online: 04 May 2024

References

1. Wood, R. J. K. Marine wear and tribocorrosion. *Wear* **376–377**, 893–910 (2017).
2. Wood, R. J. K. Tribo-corrosion of coatings: a review. *J. Phys. D: Appl. Phys.* **40**, 5502–5521 (2007).
3. Cao, S. & Mischler, S. Modeling tribocorrosion of passive metals – A review. *Curr. Opin. Solid St. M.* **22**, 127–141 (2018).
4. Watson, S. W., Friedersdorf, F. J., Madsen, B. W. & Cramer, S. D. Methods of measuring wear-corrosion synergism. *Wear* **181–183**, 476–484 (1995).
5. Wang, J., Chen, J., Chen, B., Yan, F. & Xue, Q. Wear behaviors and wear mechanisms of several alloys under simulated deep-sea environment covering seawater hydrostatic pressure. *Tribol. Int.* **56**, 38–46 (2012).
6. Traverso, P. & Canepa, E. A review of studies on corrosion of metals and alloys in deep-sea environment. *Ocean Eng.* **87**, 10–15 (2014).
7. Bueno, A. H. S. et al. Tribocorrosion evaluation of hydrogenated and silicon DLC coatings on carbon steel for use in valves, pistons and pumps in oil and gas industry. *Wear* **394–395**, 60–70 (2018).
8. Xu, Y. et al. Flow accelerated corrosion and erosion−corrosion behavior of marine carbon steel in natural seawater. *npj Mater. Degrad.* **56**, 5 (2021).
9. Tong, H. et al. Corrosion mechanism and behavior of high-velocity arc-sprayed Al–Ti–Si–RE coating in a simulated deep sea. *Mater. Corros.* **71**, 1007–1018 (2019).
10. Liu, B., Fang, Z. G., Wang, H. B. & Wang, T. Effect of cross linking degree and adhesion force on the anti-corrosion performance of epoxy coatings under simulated deep sea environment. *Prog. Org. Coat.* **76**, 1814–1818 (2013).
11. Chhowalla, M., Yin, Y., Amaratunga, G. A. J., McKenzie, D. R. & Frauenheim, T. Highly tetrahedral amorphous carbon films with low stress. *Appl. Phys. Lett.* **69**, 2344–2346 (1996).
12. Dong, C. et al. Dual-phase nanostructure of amorphous carbon and TaCB solid solution: Robust high-performance protective coating for marine equipment. *Ceram. Int.* **49**, 23153–23164 (2023).
13. Wei, J. et al. Corrosion resistance of amorphous carbon film in 3.5 wt.% NaCl solution for marine application. *Electrochim. Acta* **346**, 136282 (2020).
14. De Barros'Bouchet, M. I., Martin, J. M., Le-Mogne, T. & Vacher, B. Boundary lubrication mechanisms of carbon coatings by MoDTC and ZDDP additives. *Tribol. Int.* **38**, 257–264 (2005).
15. Sui, X. et al. Tailoring the tribocorrosion and antifouling performance of (Cr, Cu)-GLC coatings for marine application. *ACS Appl. Mater. Interfaces* **10**, 36531–36539 (2018).
16. Yamamoto, K. & Matsukado, K. Effect of hydrogenated DLC coating hardness on the tribological properties under water lubrication. *Tribol. Int.* **39**, 1609–1614 (2006).
17. Liu, Y. et al. Cr/GLC multilayered coating in simulated deep-sea environment: Corrosion behavior and growth defect evolution. *Corros. Sci.* **188**, 109528 (2021).
18. Panjan, P., Čekada, M., Panjan, M. & Kek-Merl, D. Growth defects in PVD hard coatings. *Vacuum* **84**, 209–214 (2009).
19. Ahn, S. H., Lee, J. H., Kim, J. G. & Han, J. G. Localized corrosion mechanisms of the multilayered coatings related to growth defects. *Surf. Coat. Tech.* **177-178**, 638–644 (2004).
20. Liu, Y. et al. Controllable defect engineering to enhance the corrosion resistance of Cr/GLC multilayered coating for deep-sea applications. *Corros. Sci.* **199**, 110175 (2022).
21. Panjan, P., Drnovšek, A. & Kovač, J. Tribological aspects related to the morphology of PVD hard coatings. *Surf. Coat. Tech.* **343**, 138–147 (2018).
22. Li, L. et al. Enhanced tribocorrosion performance of Cr/GLC multilayered films for marine protective application. *ACS Appl. Mater. Interfaces* **10**, 13187–13198 (2018).
23. Mirhashemihaghighi, S. et al. Interfacial native oxide effects on the corrosion protection of copper coated with ALD alumina. *Electrochim. Acta* **193**, 7–15 (2016).
24. Li, S. et al. Dense Cr/GLC multilayer coating by HiPIMS technique in high hydrostatic pressure: Microstrusctural evolution and galvanic corrosion failure. *Corros. Sci.* **225**, 111618 (2023).

25. Li, L. et al. Structural design of Cr/GLC films for high tribological performance in artificial seawater: Cr/GLC ratio and multilayer structure. *J. Mater. Sci. Technol.* **34**, 1273–1280 (2018).
26. Leppaniemi, J. et al. Effect of surface wear on corrosion protection of steel by CrN coatings sealed with Atomic Layer Deposition. *ACS Omega* **3**, 1791–1800 (2018).
27. Kong, J. Z. et al. Improved tribological properties and corrosion protection of CrN coating by ultrathin composite oxide interlayer. *Appl. Surf. Sci.* **541**, 148606 (2021).
28. Justin Kunene, T., Kwanda Tartibu, L., Ukoba, K. & Jen, T. C. Review of atomic layer deposition process, application and modeling tools. *Mater. Today.: Proc.* **62**, S95–S109 (2022).
29. Ghelich, P., Nolta, N. F. & Han, M. Unprotected sidewalls of implantable silicon-based neural probes and conformal coating as a solution. *npj Mat. Degrad.* **5**, 5 (2021).
30. Liu, M. et al. Electrochemical reactivity, surface composition and corrosion mechanisms of the complex metallic alloy Al_3Mg_2. *Corro. Sci.* **52**, 562–578 (2010).
31. Gakis, G. P. et al. Investigation of the initial deposition steps and the interfacial layer of Atomic Layer Deposited (ALD) Al_2O_3 on Si. *Appl. Surf. Sci.* **492**, 245–254 (2019).
32. Myers, T. J. et al. Smoothing surface roughness using Al_2O_3 atomic layer deposition. *Appl. Surf. Sci*. **569**, 150878 (2021).
33. Mouanga, M. & Berçot, P. Comparison of corrosion behaviour of zinc in NaCl and in NaOH solutions; Part II: Electrochemical analyses. *Corros. Sci.* **52**, 3993–4000 (2010).
34. Brug, G. J. et al. The analysis of electrode impedances complicated by the presence of a constant phase element. *J. Electroanal. Chem.* **176**, 275–295 (1984).
35. Hsu, C. H. & Mansfeld, F. Concerning the conversion of the constant phase element parameter Y_0 into a capacitance. *Corrosions* **57**, 747–748 (2001).
36. Mirhashemihaghighi, S. et al. Corrosion protection of aluminium by ultra-thin atomic layer deposited alumina coatings. *Corros. Sci.* **106**, 16–24 (2016).
37. Liu, R., Liu, L. & Wang, F. The role of hydrostatic pressure on the metal corrosion in simulated deep-sea environments — a review. *J. Mater. Sci. Technol.* **112**, 230–238 (2022).

Acknowledgements

This work was financial supported by the National Key Research and Development Program of China (2022YFB3706205), National Science Fund for Distinguished Young Scholars of China (52025014), National Natural Science Foundation of China (U20A20296), and Ningbo Science and Technology Innovation Project (2022Z054).

Author contributions

S.L.: Conceptualization, Methodology Investigation, Formal Analysis, Validation and Writing-Original. H.L.: Validation. Y.Z.: Software. W.Y.: Methodology. P.G.: Methodology Investigation, Validation. X.L.: Writing-Review & Editing. K.N.: Validation. P.K.: Editing, Funding Acquisition. A.W.: Writing-Review & Editing, Funding Acquisition, Supervision. All authors read and approved the final manuscript.

Competing interests

The authors declare no competing interests.

Additional information

Correspondence and requests for materials should be addressed to Peng Guo or Aiying Wang.